

TOWARDS A DATABASE OF MICRO-ELECTRIC MOTORS AND ELECTRONIC SPEED CONTROLLERS FOR SMALL UNCREWED AERIAL SYSTEMS

Benjamin van Magill[1] & Dries Verstraete[1]

[1]School of Aerospace, Mechanical and Mechatronic Engineering, The University of Sydney, Australia

Abstract

Flight endurance predictions for small uncrewed aerial systems (sUAS) routinely fail because constants that accurately describe motor performance across the full operating envelope are scarce or difficult to measure. The widely used three-constant motor model treats its constants as fixed motor properties, independent of drive waveform. In practice, the torque-per-amp produced by a sinusoidal motor under a six-step electronic speed controller (ESC) differs from the value the model infers from back-electromotive force (back-EMF) measurements. This paper presents an air-braked dynamometer that characterises micro-motors across their full operating envelope and uses dual alternating/direct current (AC/DC) power instrumentation to isolate motor efficiency from ESC efficiency at every operating point. This dynamometer was used to characterise ten motors across the sub-1 kg sUAS power range. In all ten cases, K_V measured below the manufacturer specification by up to 10%. The K_Q/K_E ratio is also ESC-dependent. Permanent-magnet synchronous motors (PMSMs) paired with a sinusoidal drive yield an average K_Q/K_E ratio of 1.73, consistent with theory. PMSMs paired with a six-step trapezoidal drive reduce the average to 1.53. These ten motors constitute the first entries in a validated database of sUAS propulsion constants.

Keywords: small uncrewed aerial systems, brushless motor characterisation, air-braked dynamometer, electronic speed controller, three-constant motor model

1. Motivation

Motor and ESC performance models for small uncrewed aerial systems routinely produce inaccurate endurance predictions, not because the models are wrong, but because the constants fed into them were never accurately measured. The propulsion system is the dominant power consumer in a battery-electric sUAS, and its efficiency sets the ceiling on flight time. The energy conversion chain runs from the battery through the ESC, through the motor, and finally through the propeller, with each link generating losses that accumulate into the overall efficiency. The motor and ESC are the two least well-characterised components in that chain: manufacturer-provided constants are unvalidated, and conventional dynamometers cannot cover the operating envelope required at small scale. This paper addresses motor characterisation only; ESC characterisation, enabled by the same experimental platform, is left for future work.

Inaccurate endurance predictions partially originate in the model used to derive motor constants. The three-constant motor model describes motor behaviour through a velocity constant, a zero-torque current, and a winding resistance. It is the basis for both manufacturer specifications and the majority of analytical performance predictions in the literature [1]. The model assumes these constants are fixed properties of the motor, independent of operating voltage and throttle setting. Experimental evidence shows this assumption fails: constants extracted at one operating point do not predict performance at another, and the deviations are large enough to matter for endurance estimation

[2, 3]. Accurately characterising motor constants therefore requires measurements across the full operating envelope, and this is where conventional dynamometers fall short.

Conventional dynamometer systems for small uncrewed aerial propulsion testing fall into two categories, and both have limitations that prevent full-envelope characterisation. Electromagnetic (EM) brakes generate braking torque through eddy currents or magnetic hysteresis [4, 3]. At small scale, their cogging torque introduces an offset that is large compared to the torques produced by micromotors. The maximum braking torque of EM dynamometers is also thermally limited, which causes the brake to saturate before the motor's envelope is fully explored. Propeller brakes avoid the thermal problem but sacrifice torque control. The measured operating point is entirely set by the propeller characteristic, not by the experimenter [2, 5, 6]. Neither method can independently control torque and speed across the envelope that sUAS motors operate in.

Bronz et al. proposed an alternative braking method that enables precise torque control without the thermal or cogging limitations of EM brakes [7]. They load a paddle wheel with a jet of compressed air. The concept demonstrated good measurement resolution; however, torque control was imprecise, largely because of manual adjustment of the air supply. The approach also remains mostly unvalidated in the literature. This paper builds on and improves the air-brake concept. We implement a refined dynamometer design with proportional solenoid valves for closed-loop torque control, a parametric 3D-printed paddle wheel scalable across motor sizes, and dual instrumentation to isolate motor and ESC performance independently.

The remainder of the article is organised as follows. Section 2. develops the three-constant motor model and identifies the two failure modes that define the measurement requirements. Section 3. describes the air-braked dynamometer design, including the parametric paddle wheel, instrumentation, and operating envelope. Section 4. validates the system against published data for a reference motor. Section 5. presents measured constants for ten motors and quantifies their deviation from manufacturer specifications. Section 6. summarises the findings and outlines the next steps toward a validated motor database.

2. The Three-Constant Motor Model and Its Limits

The three-constant motor model predicts motor behaviour well when its assumptions hold. Where those assumptions fail determines what the dynamometer must measure.

2.1 The Three-Constant Motor Model

A permanent-magnet brushless motor converts electrical power to mechanical power through the interaction of rotor magnets and stator windings. The rotor angular velocity rises with supply voltage and is opposed by the generated back-electromotive force (back-EMF). The equivalent circuit that formalises this treats the motor as a DC machine: an ideal motor (M) with back-EMF in series with a winding resistance (Figure 1). The back-EMF is proportional to angular velocity. The output torque is proportional to the current that flows minus a small friction-related current. The three parameters (K_V, I_0, R) characterise the model completely and are detailed below.

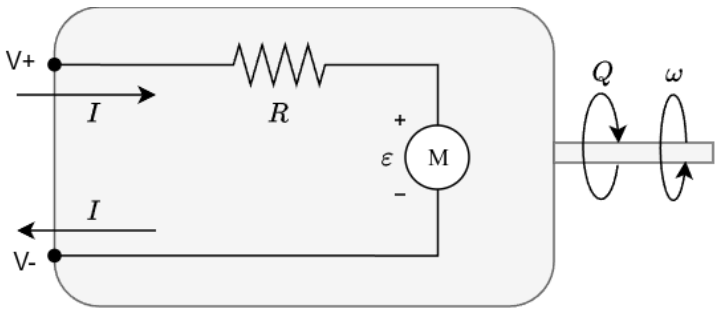


Figure 1 – Equivalent circuit for a DC electric motor

The speed constant K_V [rpm/V] relates the revolutions per minute (RPM) to the back-EMF voltage ε:

$$RPM = K_V \cdot \varepsilon \tag{1}$$

The back-EMF constant K_E [V·s/rad] expresses the same relationship in terms that link directly to the circuit. It gives the back-EMF generated per unit of angular velocity:

$$\varepsilon = K_E \cdot \omega \tag{2}$$

With appropriate unit conversion, the two constants K_V and K_E are reciprocals.
The torque constant K_Q [N·m/A] relates the electromagnetic torque Q to the motor current I:

$$Q = K_Q \cdot I \tag{3}$$

To spin the motor, some torque is lost to friction, so the shaft torque output is given by:

$$Q_{shaft} = K_Q \cdot (I - I_0) \tag{4}$$

Where I_0, referred to as the zero-torque current, is the minimum current required to spin the motor without producing any usable output. The key result here is that regardless of where torque is lost the value of K_Q does not change.
The motor resistance R [Ω] represents resistive loss in the stator windings. R determines how much of the supply voltage is lost across the windings:

$$V = \varepsilon + IR = K_E\omega + IR \tag{5}$$

For an ideal lossless motor, electrical power in equals mechanical power out. Electrical input power is given by

$$P_{\text{elec}} = \varepsilon I = K_E \omega I \tag{6}$$

while mechanical output power can be written as

$$P_{\text{mech}} = Q\omega = K_Q I \omega \tag{7}$$

Setting $P_{\text{elec}} = P_{\text{mech}}$ gives $K_E = K_Q$ directly. This result holds regardless of resistance or friction losses, and speed or torque operating point. It is a consequence of the conservation of energy, and the implication is that measuring either constant gives the other, provided the motor behaves in an ideal sense.

2.2 Where the Model Fails

The three-constant model is an idealisation for DC motors, and two of its assumptions fail in practice for motors and drive electronics typical of sUAS applications.
First, the model treats K_V, I_0, and R as fixed properties of the motor, independent of operating point. In practice, the constants can vary with DC supply voltage and throttle setting [2, 3]. Winding resistance rises with temperature while back-EMF linearity degrades at high flux density. The constants are not constants in the strict sense. They are operating-point-averaged values whose accuracy depends on how representative the averaging conditions are. A single pair of values measured at one voltage and one throttle setting might not hold across the full operating envelope.
Second, the equivalence $K_Q = K_E$ is derived for a brushless motor whose drive waveform exactly matches its back-EMF waveform. Most sUAS motors are wound for sinusoidal back-EMF as they are permanent-magnet synchronous motors (PMSM). However, low-cost ESCs drive them with a six-step trapezoidal commutation scheme. This mismatch between motor winding and drive waveform results in a reduction in the effective torque-per-amp. Back-EMF measurements (which determine K_E) are independent of the drive type and do not capture this effect. Torque measurements (which determine K_Q) do. The ratio K_Q/K_E therefore deviates measurably from unity when a six-step ESC drives a sinusoidal motor. Section 5. quantifies this deviation across the tested motors.
These two failure modes define the experimental scope. The motor constants must be measured across a representative range of voltages and throttle settings, not inferred from a single operating point. The back-EMF constant K_E must be measured independently of the drive, and the torque constant K_Q must be characterised under the ESC that will drive it in operation. The dynamometer in Section 3. satisfies these requirements.

3. Air-Braked Dynamometer Design

The air-brake principle satisfies the measurement requirements of Section 2. because braking torque is set by an impinging air jet, independently of shaft speed (Figure 2). A proportional solenoid valve controls the airflow rate to the paddle wheel blades. The dynamic pressure of the jet determines the force on the blades and, therefore, the braking torque. Against this braking torque, the motor settles at whatever speed the supply voltage and throttle dictate. Torque and speed can be varied independently across the full operating envelope, without thermal saturation and without the cogging offset that limits electromagnetic brakes at small scale.

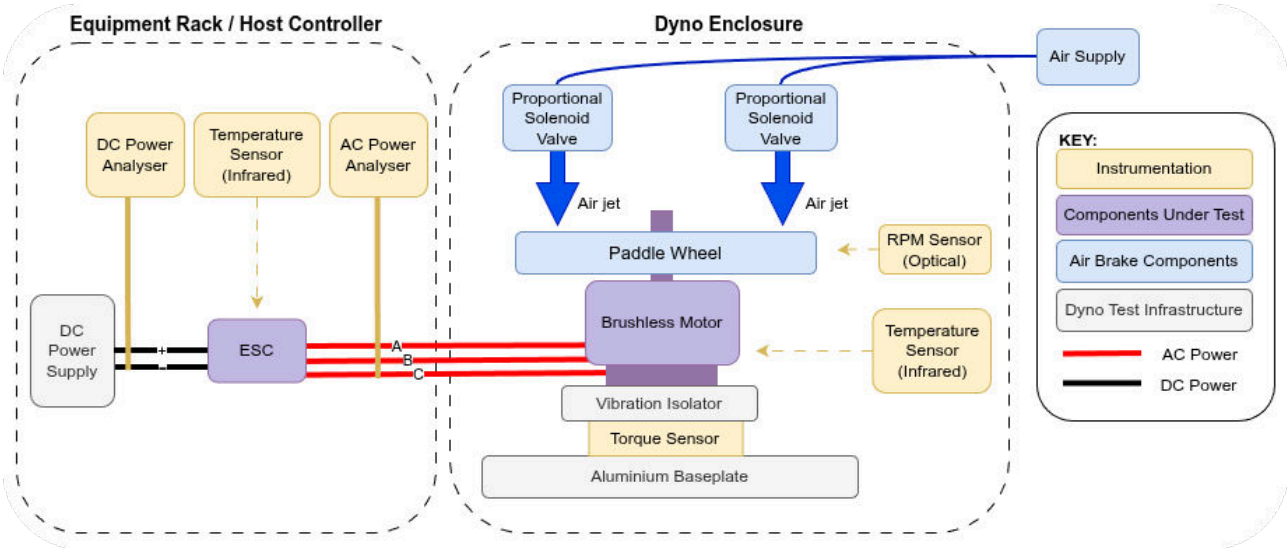


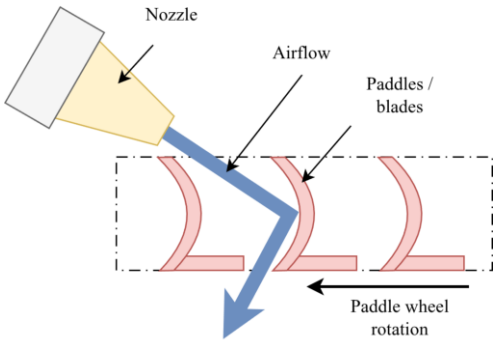
Figure 2 – Diagram of the test setup

3.1 Parametric Paddle Wheel

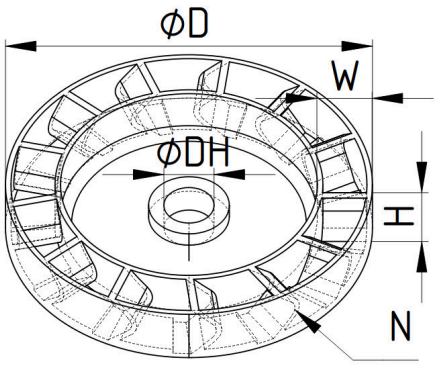
The initial paddle wheel design followed the geometry of Bronz et al. [7] and produced unacceptably high residual torque for the small motors investigated here. Residual torque, as used here, refers to the drag torque the wheel generates by rotation alone, with no airflow applied. A redesign introduced a single base plate and two thin side walls 0.9 mm thick. These walls confine each blade and direct the impinging jet to exit through a partially open base, which concentrates the braking force on the blade rather than allowing the flow to spill laterally. The confined geometry reduces residual torque and eliminates the overhanging features that require support material in 3D printing. The parametric variables that define the wheel are shown in Figure 3b and Table 1.

Table 1 – Overview of main parameters of paddle wheel depicted in Figure 3b.

Parameter	Description	Typical Value
D	Overall paddle wheel diameter	30-90 mm
DH	Hub diameter	5 mm
N	Number of paddles/blades	8-16
W	Width of paddles/blades	10 mm
H	Height of paddles/blades	10 mm



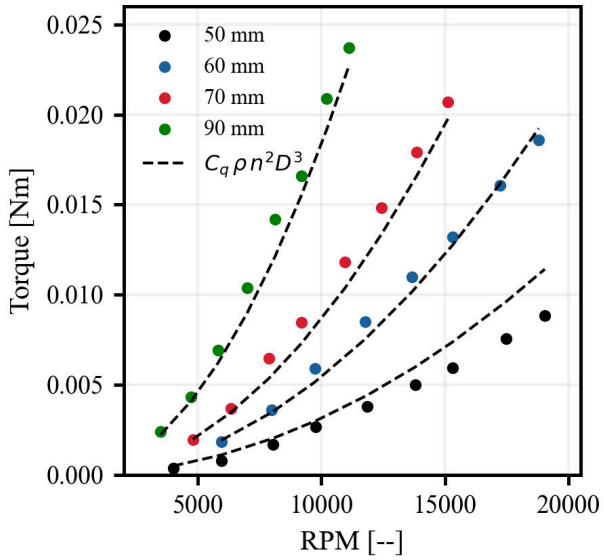
(a) Operating concept of air-braked paddle wheel



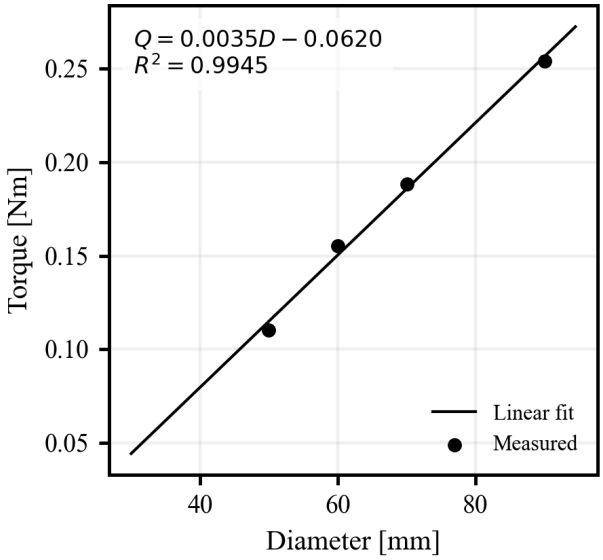
(b) Parametric paddle wheel geometry. See Table 1 for annotation details.

Figure 3 – Parametric paddle wheel

For a rotating body in which all dimensions scale with diameter, dimensional analysis yields a torque that scales as $\rho n^2 D^5$ [8]. The paddle wheel departs from this because blade dimensions W and H are fixed design parameters, independent of diameter. Each blade moves at a velocity proportional to nD and presents a fixed area WH to the flow. So the drag force per blade scales as $\rho n^2 D^2$. The torque contribution per blade equals the drag force times the moment arm and therefore scales proportional to $\rho n^2 D^3$. With blade count fixed, the total residual torque follows the same scaling. Figure 4a confirms this experimentally across diameters from 50 mm to 90 mm, with an average fit of $C_q = 7.4 \times 10^{-4}$ in the expression $Q = C_q \rho n^2 D^3$.



(a) Residual torque (no airflow) produced by paddle wheels



(b) Maximum braking torque generated by paddle wheels

Figure 4 – Torque characteristics and scaling of paddle wheels with diameter

Maximum braking torque, at full airflow, scales approximately linearly with diameter, as shown in Figure 4b. A larger wheel therefore extends the upper torque limit of the envelope, at the cost of higher residual torque at the lower end. Figure 5 compares the operating envelope of a 50 mm paddle wheel against the Magtrol HB-10 hysteresis brake used by Brown [4]. The paddle wheel provides a substantially larger operating range and is not subject to thermal limiting. Its residual torque at the maximum speed of the HB-10 is also less than half the HB-10 cogging torque. In most cases a single paddle wheel is sufficient to cover the full operating envelope of a small brushless motor with diameter selected to match the torque range of the motor under test.

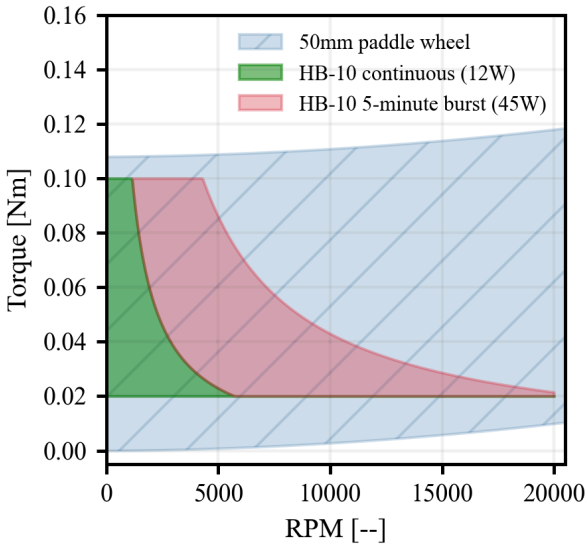


Figure 5 – Comparison of paddle wheel brake with an electromagnetic brake (Magtrol HB-10), used in studies by Brown [4]

The relationship between solenoid valve duty cycle and braking torque is non-linear. To give the experimenter direct control, the characteristic curve was measured for each valve and normalised in software, exposing an effective braking percentage as the control variable. This variable maps linearly to braking torque and can be used for open-loop sweep control or as the setpoint in a closed-loop torque controller.

3.2 Measurement and Control

Shaft torque is measured by an ATI Nano25 six-component load cell. Only the torque component is needed for motor characterisation, but the remaining components monitor vibration levels and trigger an automatic shutdown if a paddle wheel rupture is detected. Motor speed is measured by an optical sensor referenced to a high-contrast mark etched directly onto the paddle wheel side wall. A secondary electrical RPM sensor, connected to two ESC phases, serves as a backup but is limited to approximately 40,000 rpm for 14-pole motors and carries higher noise [9]. Preference is given to the optical sensor in all reported data.

On the electrical side, power is measured on both sides of the ESC. A Magtrol 6530 three-phase power analyser, combined with Hioki 3274 current probes clamped to each of the three motor phases, measures the AC power delivered to the motor (Figure 6). An Itech IT6502D programmable power supply measures the DC power supplied to the ESC. The ratio of AC output power to DC input power gives ESC efficiency, while the ratio of mechanical output power ($Q \cdot \omega$) to AC input power gives motor efficiency. The second failure mode of Section 2. requires this separation: K_Q depends on the ESC commutation waveform and must therefore be measured under the actual drive conditions, not inferred from an ideal motor using DC quantities alone.

All instruments are coordinated by a custom Python application running on a dedicated host computer, which enforces real-time safety limits and logs data. Each reported data point is the mean over a three-second measurement window. While only the mean is retained, the gradient of each channel over that window is checked to confirm that the motor and ESC have reached steady state before the reading is accepted. Standard deviations over the window are also recorded and propagated through to the final reported uncertainties in accordance with [10]. Table 2 summarises the measurement devices, their accuracy, and sample rates.

Motor temperature must be monitored to ensure that measured constants reflect a defined thermal condition. Winding resistance rises with temperature, so constants extracted at significantly different thermal states are not directly comparable. Infrared sensors monitor the motor body and ESC case temperature throughout each test, and forced air over both components provides convective cooling

during testing. A maximum temperature limit is enforced in software. If either component exceeds it, the test halts automatically and only resumes when temperatures have dropped sufficiently. The complete dynamometer hardware is also housed in an acoustic enclosure that reduces noise to levels suitable for continuous laboratory operation.

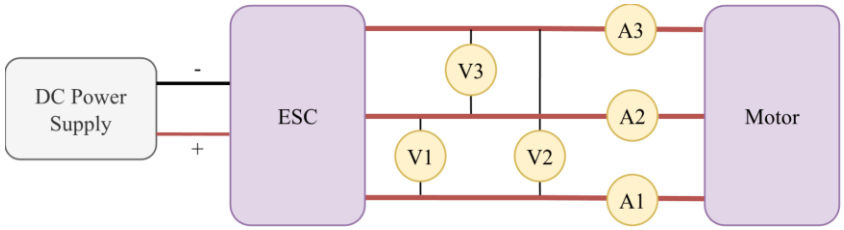


Figure 6 – Diagram showing the 3-phase voltage and current sensor connections for the Magtrol 6530 and Hioki 3274 probe

Table 2 – Summary of measurement systems used for motor and electronic speed controller testing

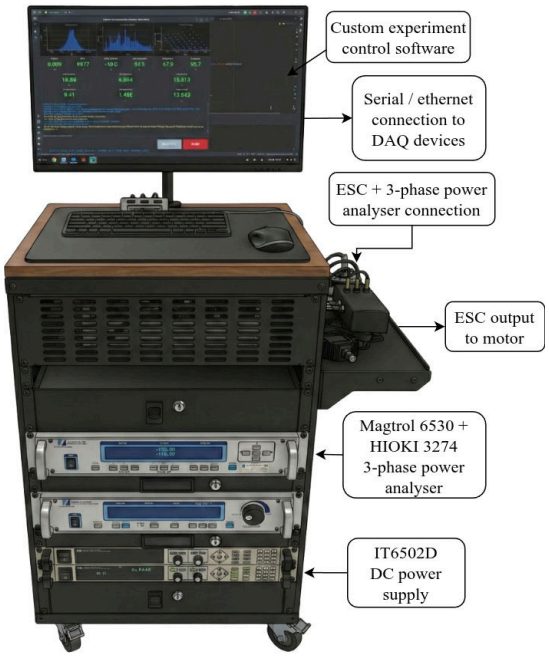
Measurement	Device	Accuracy (2σ)	Sample Rate
Torque (Q)	Nano25	$1.25\%FS$ Nm[1]	3 kHz [2]
RPM	Optical sensor	20 rpm	50 Hz
Voltage (V_{LL})	Magtrol 6530	$(0.015 \times \mathrm{F(kHz)})\%$ $+0.3\%$ Rng V [3]	250 kHz
Current (I_L)	Hioki 3274	$1\% \pm 1\mathrm{mV}$ [4]	250 kHz
Voltage (V_{DC}) Current (I_{DC})	Itech IT6502D	$0.02\% + 0.03\,\mathrm{V}$ $0.1\% + 0.06\,\mathrm{A}$	10 Hz (Host)

[1] Much greater accuracy is achieved with re-zeroing at sixty-second intervals where sensor resolution and non-linearity dominate.
[2] A 10 Hz low-pass Butterworth filter was applied to torque data.
[3] F(kHz) is the electrical commutation frequency, Rng is the variable set voltage range (e.g. 30V). Accuracy is per-phase.
[4] Probe accuracy is added to voltage input accuracy $(0.1\% + 0.2\%\ \mathrm{Rng})$ of the Magtrol 6530 in quadrature. Probe sensitivity is 0.01V/A.

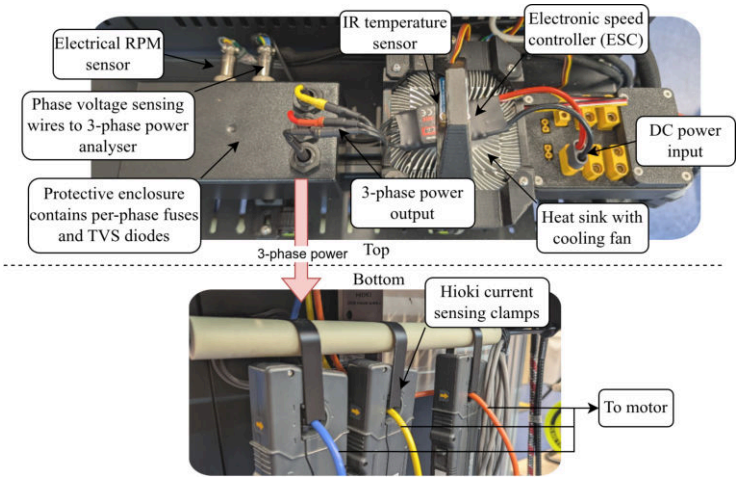
3.3 Acoustic Enclosure and System Integration

The paddle wheel generates approximately 110 dB at operating speed, which exceeds acceptable levels for continuous laboratory use. A custom enclosure was therefore built, consisting of a medium-density fibreboard shell lined internally with high-density acoustic foam [11]. The reflective shell traps sound inward, where the foam absorbs it across multiple internal reflections. Airflow exits through a baffled exhaust path sized to pass the combined mass flow from both nozzles, so that back pressure does not develop and no direct acoustic path to the laboratory is created. With the lid closed, the noise level at the operator position drops from 110 dB to 65 dB against a measurement noise floor of 55 dB.

The complete system integrates all components into a mobile equipment rack, shown in Figure 7. The rack houses the operator station, ESC wiring, and data acquisition (DAQ) hardware, while the acoustic enclosure and air brake sit alongside as a self-contained unit shown in Figure 8. The system can be quickly reconfigured for a different motor without rebuilding or rewiring between tests.

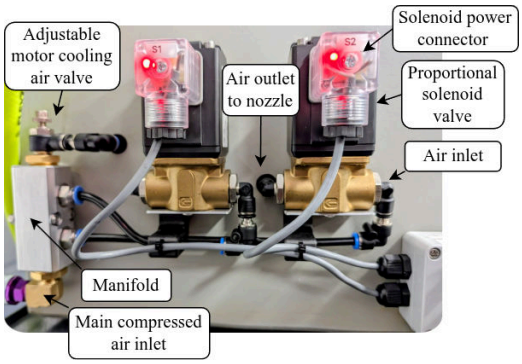


(a) Equipment rack with operator station.

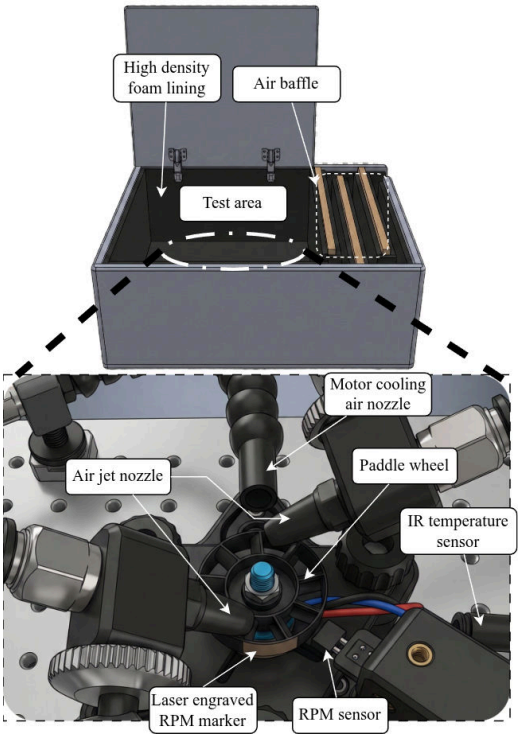


(b) ESC and 3-phase analyser wiring layout on right side shelf of rack in (a).

Figure 7 – Diagram of equipment rack with DAQ hardware.



(a) Twin proportional solenoid valve (Burkert 2875) configuration attached to the side of the enclosure in (b)



(b) Acoustic enclosure and air brake. Air baffle lid removed for clarity.

Figure 8 – Diagram of solenoid configuration and enclosure with test area.

4. Validation Against Published Motor Data

Motor performance varies with supply voltage and throttle setting, so we must measure the full envelope rather than a single point. The envelope bounds are found by setting the motor to maximum throttle and increasing braking torque until one of four limits is reached: motor stall or ESC desyn-

chronisation, maximum motor current, maximum motor temperature, or maximum braking torque output. The same procedure is repeated at minimum throttle. Once the bounds are established, test points are distributed evenly throughout and the automated sweep begins. A complete performance map at a single voltage takes approximately 15 minutes to acquire. At each point, motor efficiency is computed as

$$\eta_{motor} = \frac{Q \cdot \omega}{P_{ESC}} \tag{8}$$

where Q is shaft torque, ω is angular velocity, and P_{ESC} is the AC power delivered to the motor measured by the three-phase analyser.

The dynamometer is validated against data reported by Brown [4] for the EMAX 2213 935 K_V motor driven by a Turnigy Multistar 30A ESC at 11.1 V (Figure 9). Agreement on torque-rpm and torque-current is excellent across all throttle settings except 100%, where a difference in ESC throttle calibration between the two setups is the likely cause. The small deviation at low throttle and low torque is consistent with the HB-10 operating near its lower torque bound, as shown in Figure 5. Efficiency data show larger differences (5 to 10% for throttle settings between 50 and 90%), which reflect the sensitivity of computed efficiency to small absolute errors in torque and power at this scale rather than a systematic calibration offset. Figure 10 shows a representative performance map for the T-Motor AT2312 1150 K_V motor, illustrating the operating envelope the dynamometer resolves.

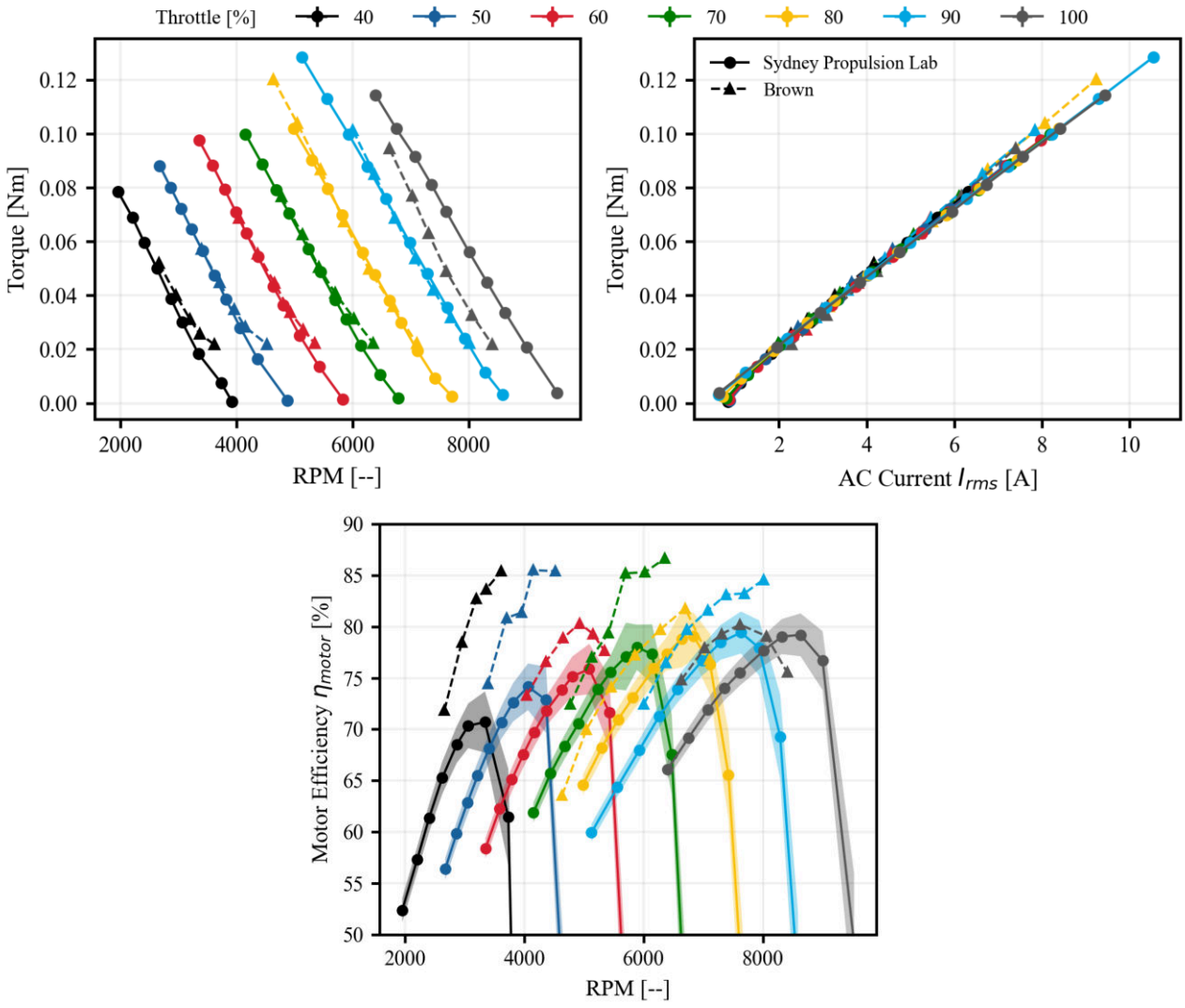


Figure 9 – Comparison of data for EMAX 2213 935 K_V with Multistar 30A ESC at 11.1 V from this research (Sydney Propulsion Lab), with Brown [4]. Shaded regions represent 1σ uncertainty.

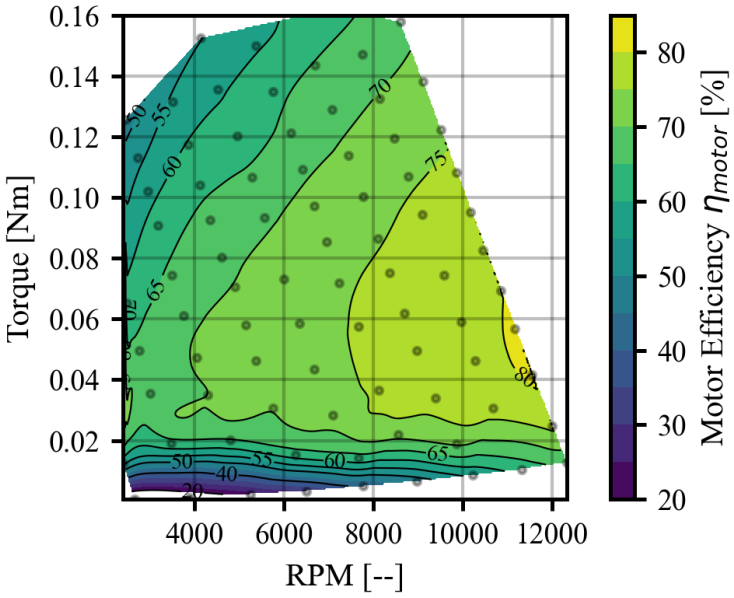


Figure 10 – Performance map of T-Motor AT2312 1150 K_V motor at 11.1 V. Efficiency contour is generated using Clough-Tocher interpolation from the measured data points (dots).

5. Measured Motor Constants and Deviation from Manufacturer Specifications

The two failure modes identified in Section 2. make testable predictions. The first predicts that K_V, I_0, and R may vary across the operating envelope, so that manufacturer specifications, which are likely derived at a single operating point, will not be representative of full-envelope behaviour. The second predicts that the ratio K_Q/K_E will deviate from unity when a six-step ESC drives a sinusoidal motor. Both predictions are tested here across ten motors displayed in Figure 11 that span the sub 1-kg sUAS power range. The measured constants for these motors form the first entries in the validated database this paper proposes.

5.1 Speed Constant and Back-EMF Constant

Two methods exist to measure K_E experimentally. The first drives the motor as a generator and records the open-circuit line-line voltage and shaft speed. The second runs the motor under its ESC at full throttle with no load. We applied both to all ten motors and use the generator method as the reference since it measures K_E as a physical motor property independent of the ESC. The open-circuit back-EMF waveform, shown in Figure 12, is sinusoidal for all motors tested, which is consistent with the PMSM construction of sUAS motors. The sinusoidal waveform fixes the RMS-to-peak conversion at $\hat{V} = \sqrt{2}V_{\mathrm{RMS}}$, within 1% of the measured ratio, and this conversion applies to all K_V comparisons that follow.



Figure 11 – Image displaying tested motors.

Table 3 presents the measured K_V and R_{LL} for all ten motors. The measured K_V is lower than the manufacturer specification in every case, with deviations of up to 10%. The two measurement methods agree within 1% across all motors, so either method is adequate when an accurate K_V is required. The line-line winding resistance R_{LL} was also measured and compared with manufacturer-provided

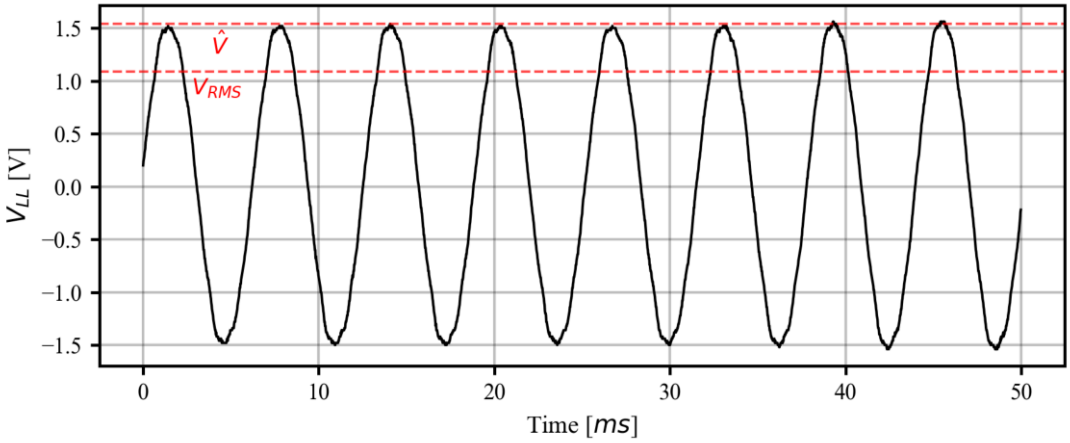


Figure 12 – Sinusoidal back-EMF waveform for a typical sUAS brushless motor

values where available, with agreement generally within 15% and the Tempest 1706 excluded as an outlier at 31%. The consistent negative bias in K_V indicates a systematic effect in how manufacturer specifications are derived. The source of this effect cannot be determined from the present data. Manufacturer specifications must not be substituted for measured values. K_V was further calculated across a number of DC input voltages using the ESC method. Figure 13 shows a K_V (and hence K_E) variation of less than 1% to the mean value across the tested voltages. K_E can therefore be considered constant.

Table 3 – Measured K_V and line-line winding resistance R_{LL} for ten sUAS motors

	K_V [RPM/$\hat{V}$]			R_{LL} [$m\Omega$]	
Motor	Provided	Tested (Back-EMF)	Tested (ESC)	Provided	Measured
ZOHD 1406	2600	2524	2523	-	394
Tempest 1704	2600	2400	2388	239	230
Tempest 1706	2370	2230	2210	170	223
Tempest 1708	1700	1551	1537	236	249
T-Motor F40 Pro II	2600	2560	2548	42	41
TBS 2207	2000	1931	1932	69	60
SunnySky 2204	1870	1835	1828	-	110
SunnySky 2212	980	890	897	123	138
EMAX 2204	2300	2163	2150	-	153
EMAX 2213	935	835	830	-	196

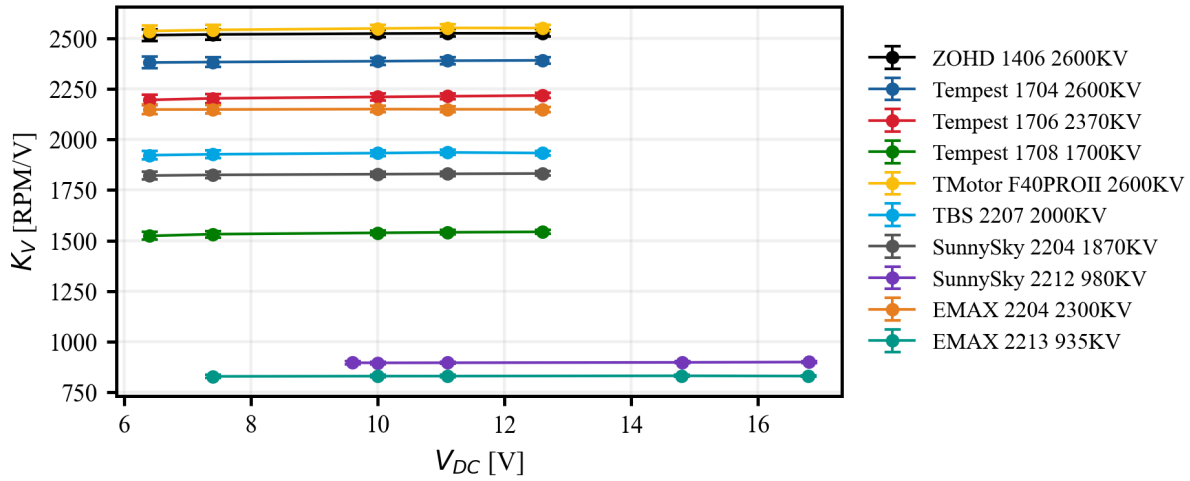


Figure 13 – Variation of K_V vs DC input voltage

5.2 Torque Constant and the K_Q/K_E Ratio

The torque constant K_Q is extracted from the slope of the measured torque-current characteristic as shown in Figure 9. To remove the effects of ESC pulse-width-modulation (PWM), only full-throttle curves were considered over several input voltages ranging from 6.4 V-16.8 V. As three-phase (motor-side) root mean square (RMS) quantities are used throughout, the relationship between K_Q and K_E depends on the drive type, as summarised in Table 4 for the ideal trapezoidal and sinusoidal cases. Two ESC types were tested: the Hobbywing Skywalker V2 20A, which uses six-step trapezoidal commutation, and the VESC EDU, which uses sinusoidal commutation. The results are shown in Table 5. The SunnySky 2212 980 K_V motor is omitted from the following lists of tested motors, as a full performance sweep was not completed.

Table 4 – Summary of important relations for trapezoidal and sinusoidal PMSM motors from [12, 13, 4]. K_Q and K_E are defined in terms of RMS quantities.

	Trapezoidal (six-step drive)	Sinusoidal
$\hat{V_{LL}}$	$\sqrt{\frac{9}{5}}V_{LL_{RMS}}$	$\sqrt{2}V_{LL_{RMS}}$
$\hat{I_L}$	$\sqrt{\frac{3}{2}}I_{L_{RMS}}$	$\sqrt{2}I_{L_{RMS}}$
Power	$2\sqrt{\frac{9}{20}}V_{LL_{RMS}}\sqrt{\frac{3}{2}}I_{L_{RMS}}$	$\sqrt{3}V_{LL_{RMS}}I_{L_{RMS}}$
$\frac{K_Q}{K_E}$	$\sqrt{\frac{27}{10}} \approx 1.643$	$\sqrt{3} \approx 1.732$

Table 5 – Measured motor constants and K_Q/K_E ratio.

Motor	ESC	K_V [RPM/$V_{LL_{RMS}}$]	K_Q [N·mm/I_{RMS}]	K_Q/K_E
ZOHD 1406		3569	4.24	1.58
Tempest 1704		3394	4.12	1.46
Tempest 1706		3154	4.82	1.59
Tempest 1708		2193	6.83	1.57
T-Motor F40 Pro II	HW Skywalker V2 20A	3620	4.11	1.56
TBS 2207		2731	5.39	1.54
SunnySky 2204		2595	5.48	1.49
EMAX 2204		3059	4.53	1.45
EMAX 2213		1181	12.41	1.53
EMAX 2213		1181	13.88	1.72
SunnySky 2204	VESC EDU	2595	6.38	1.73

With the VESC EDU, the measured K_Q/K_E ratio averages 1.73 across the two motors tested, against a theoretical value of $\sqrt{3} \approx 1.732$ for a sinusoidal drive. This close agreement validates the measurement approach. With the Hobbywing Skywalker V2 20A, the average ratio drops to 1.53, which is 7% below the theoretical trapezoidal value of 1.643. This is because a six-step ESC drives a sinusoidal motor with quasi-square-wave phase currents that do not match the ideal sinusoidal shape dictated by the back-EMF. This mismatch causes a portion of the phase current to produce zero torque while still contributing to copper losses, reducing K_Q from its ideal value. This result quantifies the second failure mode identified in Section 2.: the K_Q/K_E ratio is not a fixed motor property if the ESC commutation scheme does not match the motor back-EMF shape.

5.3 Zero-Torque Current

The zero-torque current I_0, assumed to be equal to the no-load current, appears in the three-constant model as a fixed property, yet Lundström et al. and Gong et al. report that it varies with input voltage (i.e. rotational speed) [2, 3]. This is tested here by measuring the no-load current for all motors at various voltages on both the AC and DC sides of the ESC. The results are displayed in Figure 14.
The DC-side measurements show a linear increase in $I_{0_{DC}}$ with increasing input voltage, consistent with trends reported in the literature. However, these trends do not exactly translate to the AC-side $I_{0_{RMS}}$ measurements. The T-Motor F40ProII and EMAX 2204 motors show a roughly linear increase in $I_{0_{RMS}}$ with input voltage. The rest of the motors do not. Between input voltages of 6.4V–12.6V, the TBS 2207 $I_{0_{DC}}$ varies by 0.4 A, whereas the $I_{0_{RMS}}$ value stays essentially the same (~1.1A). Other motors exhibit a similar behaviour. This inconsistency suggests that eddy-current and windage losses in most motors at this scale are negligible and could be approximated as an averaged value. The DC-side current absorbs all losses, including the ESC idle power, which could be influencing its value. Greater confidence is placed on the AC-side measurements as they reflect the actual motor-driving power.

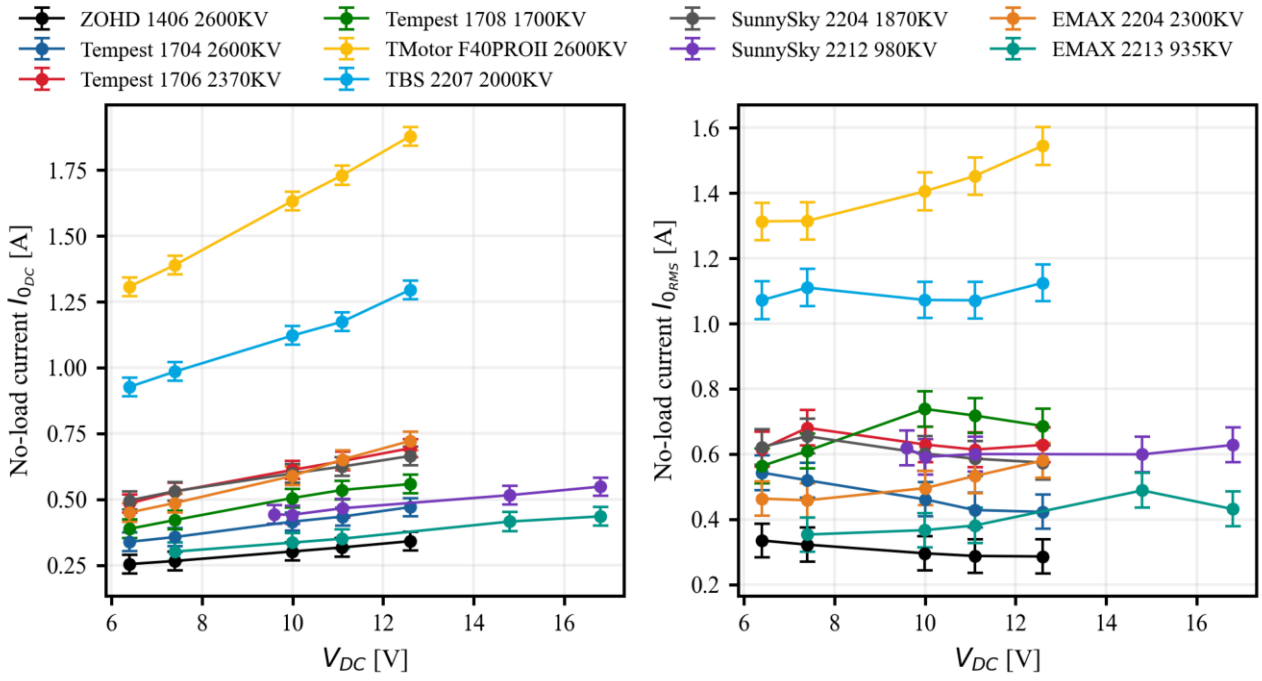


Figure 14 – Variation of I_0 vs DC input voltage for DC and AC measurements.

Moreover, the least-squares fit for the calculation of K_Q in Table 5 yielded coefficient of determination (R^2) values ranging from 0.992 to 0.999. This shows a highly linear relationship between torque and current despite the fit including measurements across all input voltages. The x-intercept of this fit also provides a constant value for I_0 in accordance with its true zero-torque definition. With these combined results, there is strong evidence that using a constant value of I_0 with AC quantities is an acceptable approximation at this scale.

Manufacturer provided I_0 is not compared here as it is typically given as a DC quantity measured at 10 V, which is not useful for modelling concerned with AC parameters only.

5.4 Three-Constant Model Fitting

The measured K_V, I_0, and R_{LL} values from the previously explored experimental methods are compared with those from a non-linear least-squares (NLLS) fit. The standard three-constant model is used, with K_Q/K_E set to the values in Table 5. The results for the tested motors are shown in Table 6. The measured values of K_V differ from the NLLS fit values by less than 2%, implying that the experimental K_V measurements are consistent and accurate. On the other hand, NLLS fit values for I_0 and R differ by a range of less than 1% up to 80%, with no clear correlation between the measured constants. In every case, I_0 from the torque vs current x-intercept method tended to under-predict the NLLS value by 20% on average, while the no-load current method over-predicted by 20% on average. The NLLS fit of R is also higher than the measured R_{LL} by an average factor of 1.44. These results indicate that no static measurement method exists to directly provide well-fitted model constants other than K_V for each motor. At this stage of investigation, characterisation with a dynamometer remains a prerequisite for high-accuracy motor modelling.

Table 6 – Comparison of motor parameters (K_V, I_0, and R) obtained experimentally and by non-linear least-squares (NLLS) estimation. Motors were paired with a Hobbywing Skywalker V2 20A ESC.

	K_V [RPM/$V_{LL_{RMS}}$]		$I_{0_{RMS}}$ [A]			R [Ω]	
Motor	Measured	NLLS	No-load	Q vs I_{RMS} x-int.	NLLS	Measured (R_{LL})	NLLS
ZOHD 1406	3569	3564	0.305	0.244	0.252	0.394	0.483
Tempest 1704	3394	3347	0.475	0.196	0.347	0.230	0.324
Tempest 1706	3154	3110	0.633	0.419	0.500	0.223	0.256
Tempest 1708	2193	2173	0.663	0.409	0.480	0.249	0.314
T-Motor F40 Pro II	3620	3628	1.406	1.385	1.408	0.041	0.075
TBS 2207	2731	2749	1.090	0.983	0.959	0.060	0.105
SunnySky 2204	2595	2598	0.607	0.456	0.509	0.110	0.168
EMAX 2204	3059	2992	0.506	0.276	0.502	0.153	0.233
EMAX 2213	1181	1176	0.404	0.273	0.316	0.196	0.271

Additionally, Figure 15 plots the experimental data against the three-constant motor model for the EMAX 2213 935 K_V using the NLLS values in Table 6. For all voltages, model estimation tracks the motor speed, torque, and efficiency within 5% of experimental values.

However, a deviation of the torque-rpm and efficiency-rpm curves emerges with increasing input voltage and current. The model tends to over-predict speed and peak efficiency at higher voltages and currents. The change in the torque-rpm slope at high voltages is partially attributed to an increase in motor temperature (and hence winding resistance R). However, the measured temperature rise of only 10°C between the lowest and highest voltage runs is insufficient to account for the discrepancy in full. I_0 has no influence on the torque-rpm slope, so it cannot resolve the difference either.

Since the torque-current fit remains accurate across all voltages, the efficiency over-prediction is a direct consequence of the speed over-prediction. No adjustment of the constants can correct the disparities without degrading the fit elsewhere. This suggests that the observed losses are beyond those explainable by resistive heating, windage, and eddy currents. Therefore, to uncover the source of discrepancy and improve the modelling fit across a broad voltage envelope, further research is required. This could include investigating a more comprehensive loss model that accounts for motor inductance or other non-idealities in the motor-ESC system.

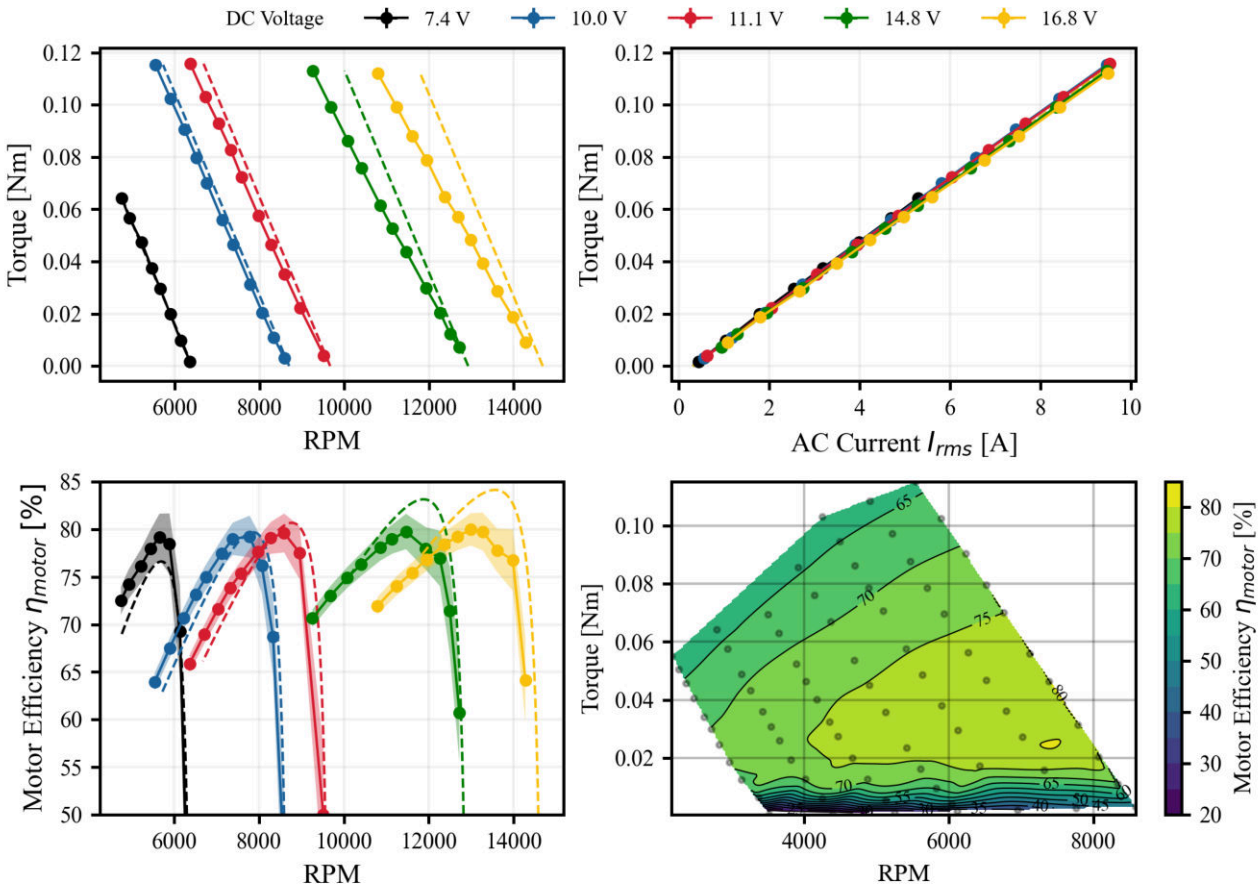


Figure 15 – EMAX 2213 935 K_V motor comparison of experimental data (solid lines) with NLLS fit three-constant model values from Table 6 (dashed lines) at full throttle. The bottom-right contour displays the operating envelope at 10V across varying throttle settings, where the dots represent raw data points. The motor was paired with a Hobbywing Skywalker V2 20A ESC.

6. Conclusions

The ten motors characterised in this paper constitute the first entries in a validated database of sUAS propulsion constants. The case for such a database is made by what these measurements reveal. The measured K_V falls below the manufacturer specification in every motor tested, by up to 10%, and measured I_0 and R values obtained using conventional methods are not guaranteed to provide the best model fit. Furthermore, the K_Q/K_E ratio depends not on the motor alone but on the motor-ESC pair. A designer who substitutes manufacturer-provided constants into an endurance model absorbs all differences without any knowledge of their magnitude. Known constants with bounded uncertainty are the precondition for trusted endurance predictions, and the measurements reported here provide them for the first ten entries.

The same dynamometer platform extends directly to ESC characterisation. The dual AC/DC power instrumentation already separates motor and ESC losses at every operating point. The K_Q/K_E ratio result demonstrates why this extension is necessary. A motor constant measured under a sinusoidal drive does not predict performance under a six-step drive. The designer does not select a motor in isolation from its ESC. The database entry that serves a designer must therefore cover a motor-ESC pair at a defined operating condition.

Ten motors are a start. The parametric paddle wheel accommodates new torque ranges without redesign, and the automated test protocol reduces characterisation time to under two hours per motor. As the database grows, the question it supports shifts from individual component constants to motor-ESC combinations that maximise range or endurance at a given operating point. That is the design question the sUAS community needs answered, and a validated database makes it tractable.

7. Contact Author Email Address

For further communication, please contact the corresponding author's email:
Ben van Magill, mailto: ben.vanmagill@sydney.edu.au

8. Copyright Statement

The authors confirm that they, and/or their company or organization, hold copyright on all of the original material included in this paper. The authors also confirm that they have obtained permission, from the copyright holder of any third party material included in this paper, to publish it as part of their paper. The authors confirm that they give permission, or have obtained permission from the copyright holder of this paper, for the publication and distribution of this paper as part of the ICAS proceedings or as individual off-prints from the proceedings.

References

[1] Mark Drela. First-order dc electric motor model. Technical report, MIT Department of Aeronautics and Astronautics, 2007.

[2] David Lundström, Kristian Amadori, and Petter Krus. Validation of models for small scale electric propulsion systems. In *48th AIAA Aerospace Sciences Meeting Including the New Horizons Forum and Aerospace Exposition*, 01 2010.

[3] Andrew Gong, Rens Macneill, and Dries Verstraete. Performance testing and modeling of a brushless dc motor, electronic speed controller and propeller for a small uav application. 07 2018.

[4] Robert H Brown. Characterisation and modeling of brushless dc motors and electronic speed controllers with a dynamometer. Master's thesis, University of Maryland, 2019.

[5] Hong-Su Nam, Seok-Hwan Lee, and Hak-Tae Lee. Electric propulsion system analysis using performance maps. *IEEE Transactions on Aerospace and Electronic Systems*, 61(4):8476–8489, 2025.

[6] M. Raju Hossain and Nicholas Krouglicof. Propeller dynamometer for small unmanned aerial vehicle. In *CCECE 2010*, pages 1–5, 2010.

[7] Murat Bronz, Jean-Marc Moschetta, and Gautier Hattenberger. Multi-point optimisation of a propulsion set as applied to a multi-tasking mav. 07 2012.

[8] Moses Frank Oduori, Jun Sakai, and Eiji Inoue. Aerodynamic torque and power on a rotating circular disc – a dimensional analysis approach. *Transactions of the Japanese Society of Agricultural Machinery*, 42, September 1993.

[9] Hobbywing Technology Co., Ltd. *Hobbywing RPM Sensor User Manual*. Hobbywing Technology Co., Ltd., 2012. Accessed 22 February 2026.

[10] John R. Taylor. *An Introduction to Error Analysis: The Study of Uncertainties in Physical Measurements*. University Science Books, Sausalito, CA, 2 edition, 1997.

[11] David A. Bies and Colin H. Hansen. *Engineering Noise Control: Theory and Practice*. Spon Press, Abingdon, UK, 4 edition, 2009.

[12] Duane C. Hanselman. *Brushless Permanent Magnet Motor Design*. Magna Physics Publishing, Lebanon, Ohio, second edition, 2006.

[13] J. R. Hendershot and Timothy John Eastham Miller. *Design of Brushless Permanent-Magnet Motors*. Magna Physics Publishing, 1 edition, 1994.